Superoxo and Peroxo Complexes on Single-Atom Catalysts: Impact on the Oxygen Evolution Reaction

Luis A. Cipriano, Giovanni Di Liberto,* and Gianfranco Pacchioni

ACCESS | Metrics & More | Article Recommendations | Supporting Information
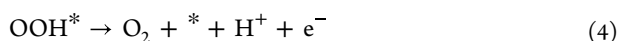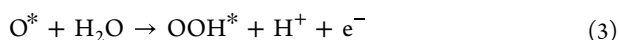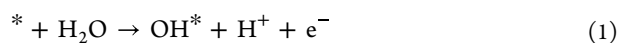
ABSTRACT: In this work, we demonstrate the essential role of the formation of superoxo and peroxo complexes on single-atom catalysts (SACs), an aspect that is often neglected in the study of these systems. By means of density functional theory calculations, we consider a representative set of 11 transition metal atoms (Sc, V, Ti, Cr, Mn, Fe, Co, Ni, Cu, Pd, Pt) anchored on nitrogen-doped graphene, and we show that most of them form stable superoxo and peroxo intermediates when they react with molecular oxygen. Their formation has a direct impact on the oxygen evolution reaction (OER), and we develop the corresponding microkinetic models showing that this step of the reaction cannot be neglected. Depending on the transition metal atom, the inclusion of the superoxo/peroxo complexes in the analysis of the reaction profile can change the kinetics by several orders of magnitude. This work reveals the important role of dioxygen complexes species in the OER and reinforces the notion of SACs as analogs of coordination compounds.

KEYWORDS: OER, superoxo, peroxo, complexes, DFT, SACs
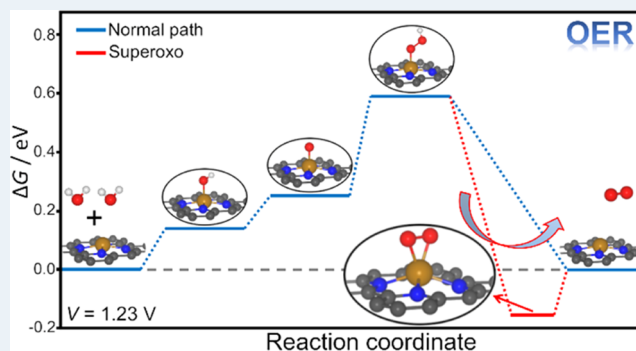
1. INTRODUCTION

Water splitting is probably one of the most studied catalytic reactions in recent years.[1−4] With this reaction, water can be converted into molecular oxygen and hydrogen, that, in turn, can be used as an energy vector. The thermodynamic cost of the $2H_2O \rightarrow 2H_2 + O_2$ process is 4.92 eV. At the cathodic site of an electrolyzer, the hydrogen evolution reaction (HER) occurs, $4H^+ + 4e^- \rightarrow 2H_2$, while at the anodic site, the oxygen evolution reaction (OER) takes place, $2H_2O \rightarrow O_2 + 4H^+ + 4e^-$. HER usually occurs on metals via the formation of an intermediate characterized by a hydrogen atom adsorbed on the catalytic site.[5,6] The mechanism of OER is much more complex and involves the formation of several intermediates. Usually, it is assumed that OER starts from the formation of an adsorbed OH group on the catalytic site *; this converts into O and further to OOH, which finally releases O_2[7−9]

$$* + H_2O \rightarrow OH^* + H^+ + e^- \quad (1)$$

$$OH^* \rightarrow O^* + H^+ + e^- \quad (2)$$

$$O^* + H_2O \rightarrow OOH^* + H^+ + e^- \quad (3)$$

$$OOH^* \rightarrow O_2 + * + H^+ + e^- \quad (4)$$

Notice that in these reaction steps, adsorbed O_2 species (peroxo, O_2^{2-}, or superoxo, O_2^-) are not present, as it is usually assumed that the above reactions take place at a metal electrode where these species do not form. The Gibbs energy

of HER is equal to 0 eV in standard conditions, and consequently, the cost for OER is 4.92 eV, which is also the cost for the entire water splitting reaction. Unfortunately, the energy effectively required for the reaction is higher due to the presence of overpotentials.

Among the best catalysts for this reaction is platinum.[10] It has a nearly zero overpotential for HER and a moderate overpotential for OER, making the reaction slow. Heard and Lennox reported an overpotential of 0.46 V measured at 1 mA/cm².[11]
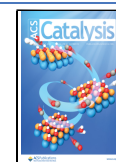
A possible explanation for this experimental observation is based on the fact that the calculated Gibbs energy of the OER intermediates differs from the ideal value. For instance, the calculated Gibbs energy cost to form OOH from OH is about 3.2 eV, around 0.8 eV higher than the ideal value (2.46 eV).[9,12]

Several studies have been dedicated to the search for novel catalysts beyond bulk metals, with the aim of minimizing the overpotential of OER.[13−15] In particular, great attention has been dedicated to catalysts with reaction profiles different from the conventional one, where nonelectrochemical reaction steps

ACS Publications
© 2022 The Authors. Published by
American Chemical Society
11682
https://doi.org/10.1021/acscatal.2c03020
ACS Catal. 2022, 12, 11682−11691

take place. For instance, the lattice oxygens of perovskite (ABO_3) oxides can take part in the reaction lowering the overpotential.[16−18] The participation of lattice oxygens with the formation of oxygen vacancies in the catalytic processes is common in catalysis, as in the Mars−van Krevelen mechanism.[19,20] Also, surface oxygen atoms can stabilize the conventional OER intermediates by promoting some rearrangement, as demonstrated on RuO_2 (110) surfaces.[21−23]

Metal single atoms stably anchored on a support are among the most studied alternatives to extended metal surfaces for water splitting.[15,24−27] Single-atom catalysts (SACs) are the bridge between heterogeneous and homogeneous catalysis, making it possible to fully exploit the amount of catalytic sites.[28−31] Furthermore, the chemistry of a metal single atom differs from that of a bulk metal[32,33] and can be tailored by engineering the local coordination, opening in principle several possibilities to improve the catalytic activity. The chemistry of SACs is usually complex and reminiscent of that of coordination chemistry compounds. Indeed, reaction intermediates that would be unstable on metal electrodes may be stable on a SAC, with direct consequences on the efficiency of the process.[34] For instance, we recently showed that stable dihydrogen intermediates form on SACs, at variance with metal surfaces, with an important impact on the kinetics of the HER.[35] Similarly, dioxygen species can form on SACs, giving rise to superoxo/peroxo complexes. The existence of these species is well known in coordination chemistry.[36−38] It is enough to mention the formation of the heme−superoxo complex, responsible for the oxygen transport in the blood.[39,40] On SACs, complexes have been experimentally observed in a few studies devoted to the oxygen reduction process[41,42] and also emerged from computational studies[43−45] where the elongation of the O−O bond distance was shown to boost the O_2 reduction kinetics.[46] For OER, a common strategy is to transfer the knowledge from metal and oxides, assuming that the reaction occurs on SACs via the well-known path OH*, O*, and OOH*. Consequently, the formation, importance, and impact on the kinetics of the process of superoxo and peroxo complexes have not been emphasized so far and represent the main messages of this work. It is important to mention that such species have also been observed on some heterogeneous catalysts or mixed homogeneous/heterogeneous catalysts through the formation of intramolecular oxygen coupling between two adjacent metal sites.

We will show that (i) the formation of superoxo/peroxo species on SACs is a thermodynamically favorable event on several transition metals (TMs), and (ii) when superoxo/peroxo complexes form, this has relevant implications on the OER performance so that they must be included in the analysis of the reaction mechanism. In particular, this second aspect is of key importance for the correct screening of potentially interesting catalytic systems based on computational studies. For this purpose, we performed density functional theory (DFT) calculations on metal single atoms embedded in nitrogen-doped graphene, a widely studied catalytic system.[27,47−50] We have investigated the OER including the new superoxo/peroxo intermediate on first-row transition metals (Sc, Ti, V, Cr, Mn, Fe, Co, Ni, Cu), stabilized in N-doped graphene, with the addition of Pd and Pt as these are among the most studied SACs.[27,47−50] Of course, when the goal of the simulation becomes the experimental design of new catalysts, one should also consider the relative stability of the carbonaceous support in operative conditions.

The work is organized as follows. After a brief description of the computational details, we show that in 7 cases out of 11, stable superoxo/peroxo complexes form when O_2 is added to the system, and we discuss the nature and structure of these species. Next, we discuss the Gibbs energy profiles for OER including the new intermediate to demonstrate its importance. Last, based on a simple microkinetic model, we provide quantitative estimates of the impact that the formation of the superoxo/peroxo complexes has on the kinetics of OER. We finally mention our purpose is not to predict the catalytic performances of specific SACs but rather to highlight the importance of the superoxo/peroxo complexes when modeling OER on SACs.

2. COMPUTATIONAL DETAILS

Spin-polarized DFT calculations have been performed with the VASP 6.2[51−53] code using the generalized gradient approximation (Perdew−Burke−Ernzerhof (PBE) functional).[54] Dispersion terms have been introduced using the D3 Grimme's parametrization.[55]

The valence electrons treated explicitly are: H (1s), C (2s,2p), N (2s, 2p), O (2s, 2p), Sc (3p, 4s, 3d), Ti (3p, 4s, 3d), V (3p, 4s, 3d), Cr (3p, 4s, 3d), Mn (3p, 4s, 3d), Fe (4s, 3d), Co (4s, 3d), Ni (4s, 3d), Cu (4s, 3d), Pd (5s, 4d), and Pt (6s, 5d). They have been expanded by a set of plane waves with a kinetic energy cutoff of 400 eV, whereas the core electrons were treated with the projector augmented wave approach.[56,57] The convergence criteria for electronic and ionic loops were set to 10^{-6} eV and 10^{-3} eV/Å, respectively. A $5 \times 5 \times 1$ Monkhorst−Pack k-point grid was used.[58]

We considered a nitrogen-doped graphene layer where a C divacancy has been created, four C atoms have been replaced by four N atoms, and a TM atom has been embedded in this coordination site, TM@4N-Gr (pyridine coordination). The supercell of 4N-Gr contains 32 atoms and has lattice parameters a, b, and γ equal to 9.87 Å, 9.87 Å, and 120°, respectively.[32,59] The atomic coordinates have been fully relaxed for each of the SACs considered.

One problem related to the theoretical description with DFT of TM atoms with localized orbitals is the self-interaction error inherent to standard GGA functionals. One possible way to reduce this problem is to adopt hybrid functionals,[60] although this may imply an increase in the computational burden. A cheaper alternative consists in the adoption of the Dudarev's GGA + U approach,[61,62] which, however, has the problem that the results depend on the choice of the U parameter. In addition, tuning U also implies other effects related to charge localization. Therefore, the origin of the U term should be justified. Usually, it can be tuned to fit a relevant quantity. In the semiconductors' field, it is possible to determine U to better reproduce the band gap of the material.[63] In the field of SACs, we found several literature works[47,64,65] adopting U values derived from a study of Anisimov and co-workers.[66] This aspect was discussed in more detail elsewhere.[67] We decided to adopt the same values (see the SI for the U values). Despite these limitations, besides the main set of GGA results that will be presented below, we also performed some test calculations with GGA + U to evaluate the impact on the stability of superoxo/peroxo species. The GGA + U results are qualitatively in agreement with the GGA ones. Some relevant quantitative differences are found in specific cases, which points to the importance of the choice of the correct DFT approach for accurate predictions of the

catalytic activity of SACs. This depends on the number of unpaired electrons associated with a specific SAC. This is an important warning when screenings of potential candidates for OER are done based on large sets of systems investigated at the GGA level.[67] The conclusions could be substantially different using hybrid functionals or the GGA + U approach. Nevertheless, for the purpose of this work, i.e., demonstrating the importance of the formation of the superoxo/peroxo complexes, the use of GGA or GGA + U methods is less relevant as this impacts the absolute values of the energy terms, not the general trends, see Table S1. Addressing this aspect goes beyond the purpose of this study, and for this reason, the discussion reported below is based on GGA results only, keeping in mind that a comparison of different approaches is needed for a quantitative study of SACs in OER.

3. RESULTS AND DISCUSSION

3.1. Structure and Stability of Superoxo/Peroxo Complexes.
The formation of superoxo and peroxo complexes on SACs is not a rare event. We adsorbed molecular oxygen on the 11 SACs described above, and we considered two possible isomers, "end-on" (η^1) or "side-on" (η^2), according to classical inorganic chemistry textbooks, Figure 1.[68]
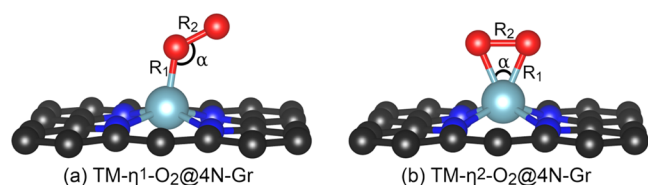

Figure 1. Oxygen complexes on TM atoms embedded in N-doped graphene, TM@4N-Gr. (a) "end-on" and (b) "side-on" oxygen complexes.

The adsorption Gibbs energy has been computed with respect to molecular oxygen (O_2) and the free catalyst (TM@4N-Gr, labeled as *)

$$* + O_2 \rightarrow O_2* \tag{5}$$

$$\Delta E_{\eta^n-O_2} = E_{O_2*} - (E_* + E_{O_2}) \tag{6}$$

$$\Delta ZPE_{\eta^n-O_2} = ZPE_{O_2*} - (ZPE_* + ZPE_{O_2}) \tag{7}$$

$$T\Delta S_{\eta^n-O_2} = T(S_{O_2*} - (S_* + S_{O_2})) \simeq -TS_{O_2} = -0.64 \text{ eV} \tag{8}$$

$$\Delta G_{\eta^n-O_2} = \Delta E_{\eta^n-O_2} + \Delta ZPE_{\eta^n-O_2} - T\Delta S_{\eta^n-O_2} \tag{9}$$

Full details related to entropic and zero-point energy terms can be found in the SI. Please note that the vibrational entropy of solid-state species is neglected, and this leads to uncertainties in the Gibbs energies as high as 0.2 eV, see the SI, which is comparable with the typical error of DFT energies.

R. E. Berry demonstrated that several transition metals form complexes with O_2, and many of these complexes form reversibly.[68] The structure of these compounds is usually evaluated by single-crystal X-ray crystallography. Moving to our results, in seven cases, energetically stable complexes form, see Table 1. The binding energies show a great variability; Sc, Ti, V, and Cr form extremely stable complexes, with a Gibbs energy of more than 1 eV; Mn, Fe, and Co bind O_2 more weakly. Interestingly, the reactivity of Fe@4N-Gr reminds that of porphyrin-based adducts.[69−71] Transition metal atoms at the right of the periodic table (Ni, Cu, Pd, and Pt) do not form adducts with O_2.

The relative stability of η^1 and η^2 complexes varies substantially depending on the TM atom, Table 1. On Sc, only the side-on (η^2) complex forms; side-on is also the preferred form for Ti and V. On Cr and Mn, the η^1 and η^2 complexes are nearly isoenergetic, while the end-on (η^1) complex becomes the ground state structure on Fe and Co. This trend is well illustrated in Figure 2 where the energy difference between the two possible configurations, $\Delta E(\eta^2-\eta^1)$, is plotted versus the TM atom.
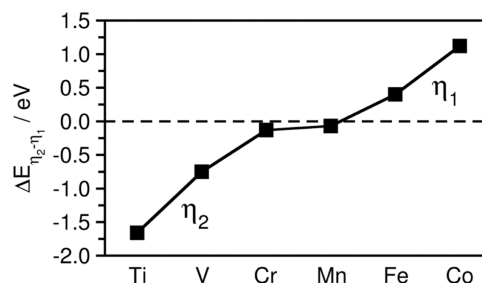

Figure 2. Energy difference between the two possible superoxo/peroxo configurations, $\Delta E(\eta^2 - \eta^1)$, formed on TM@4N-Gr (TM = Ti, V, Cr, Mn, Fe, and Co).

Moving to structural aspects, Table 1, the O−O bond distance is elongated by 5−6.5% with respect to O_2 (1.23 Å) in η^1-O_2 complexes and by about 10−20% in η^2-O_2 complexes. Our values can be compared with available data for other dioxygen adducts. Armillotta et al. characterized dioxygen

Table 1. Structural Parameters of η^1-O_2 and η^2-O_2 Complexes on TM@4N-Gr[a,b]

TM-η^1−O_2@4N-Gr						TM-η^2−O_2@4N-Gr					
TM	d_{N-TM}	R_1	R_2	α	ΔE	ΔG	TM	d_{N-TM}	R_1	R_2	α	ΔE	ΔG
Sc							Sc	2.18	2.02	1.41	40.66	−3.20	−2.56
Ti	2.06	1.73	1.31	178.95	−3.14	−2.50	Ti	2.08	1.84	1.46	46.66	−4.80	−4.16
V	2.02	1.69	1.30	179.03	−2.93	−2.29	V	2.06	1.82	1.48	47.97	−3.68	−3.04
Cr	1.97	1.77	1.31	126.07	−1.64	−1.00	Cr	2.02	1.84	1.43	45.79	−1.77	−1.13
Mn	1.95	1.82	1.30	118.62	−0.91	−0.27	Mn	2.01	1.84	1.41	45.04	−0.98	−0.34
Fe	1.92	1.77	1.29	120.66	−1.01	−0.37	Fe	2.00	1.85	1.39	44.14	−0.61	0.03
Co	1.91	1.87	1.29	118.07	−0.85	−0.21	Co	1.97	1.90	1.35	41.67	0.27	0.91

[a]R_1 and R_2 correspond to the TM−O, O−O bond distances (in Å) in the complexes and α to the angle, see also Figure 1. [b]Adsorption energies and free energies, ΔE and ΔG, are reported in eV.
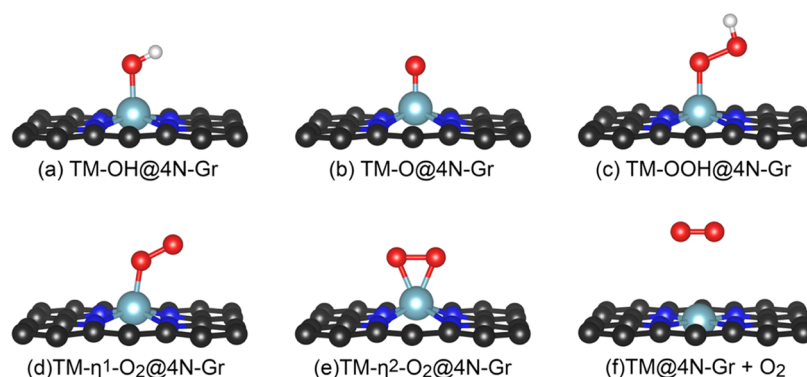
Figure 3. Structures of OER intermediates on a TM atom embedded in N-doped graphene (TM@4N-Gr). (a) OH, (b) O, (c) OOH, (d) η^1-O_2, (e) η^2-O_2, and (f) O_2 release.

species in a cobalt 2D metal-organic frameworks,[72] finding that a η^1-O_2 complex has a Co–O distance of 2.2 Å, an O–O bond of 1.27 Å, and a Co–O–O angle of 118°. These values are consistent with our findings for Co, see Table 1. As already mentioned, the Fe–O$_2$ complex has been widely studied in the past, in particular the Fe-porphyrin derivatives,[71] myoglobin,[69,70] heme-and-homo-proteins,[73,74] tetra-N-heterocyclic-carbene,[75] and tetraamido macro-cyclic ligands.[76] In these studies, the Fe–O bond distance spans from 1.80 Å to 1.87 Å, the O–O one from 1.24 Å to 1.34 Å, and the Fe–O–O angle from 118° to 125°. These values are in line with our findings for Fe@4N-Gr, Table 1, and Figures S1, S2. Therefore, stable superoxo/peroxo species can form on SACs with structural characteristics similar to those of the corresponding inorganic complexes. η^1 and η^2 complexes display relevant differences. The analysis of O–O bond distance (R_2 in Table 1) indicates that η^1 complexes have a superoxo character, and η^2 compounds are peroxo species. This is further corroborated by the analysis of spin density and states, see Figure S4, where, as expected, peroxo species do not have unpaired electrons, differently from superoxo ones having residual spin density associated with approximately one unpaired electron.

3.2. Implications of Superoxo and Peroxo Complexes for OER. In this section, we discuss the implications that the formation of superoxo/peroxo intermediates has on the OER. We evaluate the Gibbs energy reaction profiles assuming that the OER reaction proceeds via the three monoelectronic steps reported in eqs 1–3; then, we introduce the additional electrochemical step corresponding to the formation of the superoxo/peroxo complex (O_2^*), eq 10, followed by O_2 release (nonelectrochemical), eq 11

$$OOH^* \rightarrow O_2^* + H^+ + e^- \tag{10}$$

$$O_2^* \rightarrow ^* + O_2 \tag{11}$$
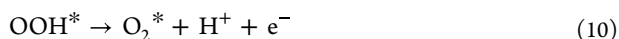
It is worth mentioning that other paths are possible for OER on SACs. These imply the formation of other intermediates than those reported in eqs 1–3, like for instance a TM(OH)$_2$ complex where two hydroxyl groups are simultaneously bound to the active center.[77] However, for the purpose of this work, considering the most common path is sufficient; Figure 3 shows the side view of the atomistic structure of the intermediates involved in the OER. The computed Gibbs energy for each intermediate, Table 2, has been obtained using the set of equations reported in Section 2 of the SI. Given that the bond strength of O_2 is not properly reproduced at the PBE

Table 2. Adsorption Gibbs Energy of OH, O, OOH, and O_2 Complexes on TM Atoms Embedded in N-Doped Graphene, TM@4N-Gr (ΔG, in eV)[a]

TM	ΔG_{OH}	ΔG_O	ΔG_{OOH}	$\Delta G_{\eta^1-O_2}$	$\Delta G_{\eta^2-O_2}$	ΔG_{O_2}
Sc	−3.18	−2.00	−2.26		−2.92	0.00
Ti	−3.33	−4.59	−4.66	−2.86	−4.53	0.00
V	−2.62	−4.39	−4.52	−2.65	−3.41	0.00
Cr	−1.27	−2.54	−0.41	−1.36	−1.50	0.00
Mn	−0.60	−1.41	0.14	−0.63	−0.71	0.00
Fe	−0.56	−0.97	0.05	−0.73	−0.34	0.00
Co	−0.15	0.18	0.64	−0.57	0.54	0.00
Ni	0.87	1.59	1.31			0.00
Cu	0.73	1.70	1.28			0.00
Pd	1.20	2.23	1.65			0.00
Pt	1.31	2.04	1.56			0.00

[a]Values are calculated at $V = 1.23$ V (see text).

level, this would lead to an incorrect estimate of the overall OER Gibbs energy. A possible strategy to overcome this problem is to adopt the experimental reference value, 4.92 eV. Values are reported assuming to apply a voltage $V = 1.23$ V.

Figure 4 shows the Gibbs energy profiles for the OER, where the most stable complex (side-on or end-on) is reported for each SAC. In some cases, Cr, Mn, Fe, and Co, the inclusion of the step in eq 10 implies the appearance of an additional reaction barrier. The release of O_2 from the OOH intermediate is exergonic for Fe, Mn, and Co, and nearly exergonic for Cr, if one neglects the superoxo/peroxo complex formation, but this is no longer the case if one includes superoxo/peroxo formation. For Sc@4N-Gr, the formation of the complex implies an increase in the reaction barrier for O_2 release, while for Ti@4N-Gr and V@4N-Gr, the formation of the complex results in an intermediate with Gibbs energy between that of the OOH complex and the O_2 desorption step. This shows that the energy profiles can change substantially when the formation of the superoxo and peroxo species is considered explicitly. A further proof of the large changes in the reaction Gibbs energy profiles can be obtained by evaluating the maximum reaction barrier (η) as a function of the applied voltage V. In reactions characterized only by electrochemical steps, the value of V at which $\eta = 0$ corresponds to the limiting potential. It is important to mention that, when considering superoxo/peroxo complexes, the last step (eq 11) does not involve electron exchange and thus is voltage-independent. If the complex is more stable than the free oxygen molecule, a
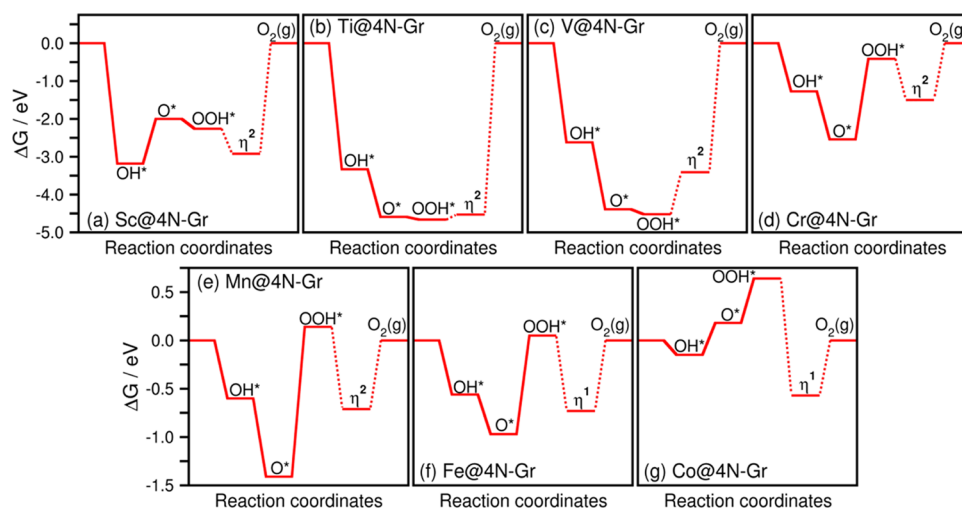
Figure 4. Gibbs energy profiles for the OER (a) Sc@4N-Gr, (b) Ti@4N-Gr, (c) V@4N-Gr, (d) Cr@4N-Gr, (e) Mn@4N-Gr, (f) Fe@4N-Gr, and (g) Co@4N-Gr, at V = 1.23 V.
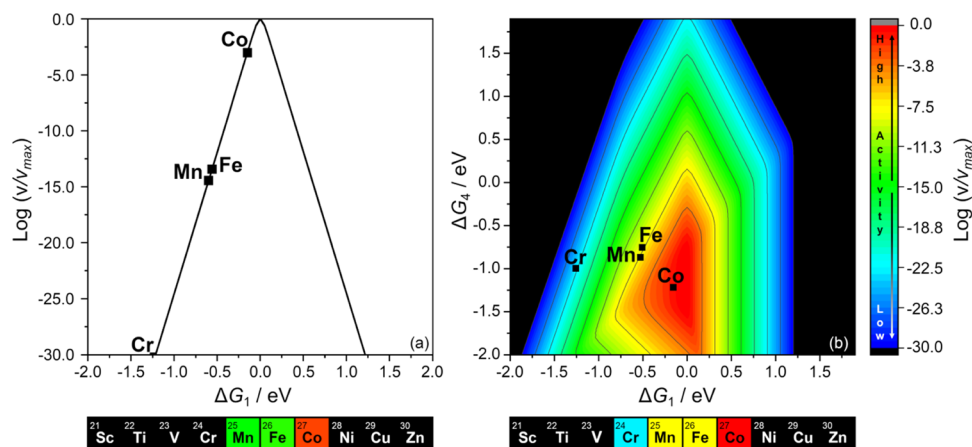

Figure 5. (a) Two-dimensional volcano plot for the OER reaction (at V = 1.23 V) based on the formation of the MOH intermediate (simple microkinetic model, see text); the solid line corresponds to the analytic solution of eq 16; the DFT computed values for Cr, Mn, Fe, and Co are reported and lie along this analytical curve; (b) three-dimensional volcano plot for the OER reaction assuming the formation of a superoxo/peroxo complex (new microkinetic model proposed here), eq 17. Color meaning: red, high activity; blue, low activity. When $\log(v/v_{max}) < -30$ (extremely low activity), the color is black. In the two plots, we reported intermediates with ΔG_1 and ΔG_4 between -2.0 and 2.0 eV.

positive barrier will always be present. Table S6 reports the maximum applied voltage at which the inclusion of superoxo/peroxo complexes implies reaction barriers lower than or equal to those obtained neglecting the formation of the complexes.

The analysis of the Gibbs energy diagrams allows us to draw some qualitative conclusions in terms of limiting steps, favorable or unfavorable process, etc. However, quantitative estimates can be provided only by accounting for microkinetic models including the formation of the additional intermediate. In the last section, we address this aspect by providing a comparison of two simple kinetic models, with and without the presence of superoxo/peroxo complexes.

3.3. Microkinetic Modeling. In this section, we construct a simple microkinetic model based on the Butler–Volmer formalism to take into account the formation of the superoxo and peroxo complex. We would like to stress that the main purpose is simply to demonstrate the impact of considering superoxo/peroxo complexes on the kinetics of the reaction. Of course, modeling the reaction kinetics requires more accurate models that include the kinetic barriers. Here, we adopt the Nørskov approach in which the reaction barriers different from

those of thermochemistry are neglected. This model was very successful over the years.[78,79] The typical OER pathway implies the formation of three intermediates (OH, O, OOH) and follows eqs 1−4. This gives rise to three equations to describe the respective reaction rates

$$v_1 = k_1\Theta_* e^{-\beta\Delta G_1/k_bT} \quad v_{-1} = k_{-1}\Theta_{OH^*} e^{(1-\beta)\Delta G_1/k_bT} \quad (12)$$

$$v_2 = k_2\Theta_{OH^*} e^{-\beta\Delta G_2/k_bT} \quad v_{-2} = k_{-2}\Theta_{O^*} e^{(1-\beta)\Delta G_2/k_bT} \quad (13)$$

$$v_3 = k_3\Theta_{O^*} e^{-\beta\Delta G_3/k_bT} \quad v_{-3} = k_{-3}\Theta_{OOH^*} e^{(1-\beta)\Delta G_3/k_bT} \quad (14)$$

Here ΔG_1, ΔG_2, and ΔG_3 are the free energies associated with the steps reported in eqs 1−3. The velocity of the overall reaction is

$$v_4 = k_4\Theta_{OOH^*} e^{(1-\beta)(\Delta G_1 + \Delta G_2 + \Delta G_3)/k_bT} \quad (15)$$

assuming to work at the ideal applied potential V = 1.23 V and pH = 0. The problem depends on three different variables (see the SI) associated with the stability of OH, O, and OOH

Table 3. Calculated Activities of SACs Obtained Without and With Inclusion of the Formation of a Superoxo/Peroxo Complex in the Kinetic Model[a,b]

	without superoxo/peroxo	with superoxo/peroxo	
	$\log(v_1)$	$\log(v_2)$	v_2/v_1
Sc@4N-Gr	−79.83	−74.55	1.91×10^5
Ti@4N-Gr	−83.63	−85.03	3.98×10^{-2}
V@4N-Gr	−65.63	−75.31	2.09×10^{-10}
Cr@4N-Gr	−31.41	−22.50	8.13×10^8
Mn@4N-Gr	−14.43	−8.69	5.50×10^5
Fe@4N-Gr	−13.42	−8.59	6.76×10^4
Co@4N-Gr	−3.03	−0.79	1.74×10^2

[a]In both cases, the maximum corresponds to $\log(v) = 0$. [b]The last colon reports the ratio of the two velocities and provides a measure of the increase or decrease in the predicted activity.

intermediates. If we impose the scaling relationships for O* and OOH*,[5,9,80] everything becomes dependent on the Gibbs energy of the OH intermediate, and the problem reduces to one dimension. The scaling equations have been taken from seminal works of Koper's and Calle-Vallejo's groups (see the SI for full details).[5,9,80] Some evidence has been reported recently for SACs as well.[81] Similar results are obtained with only minor numerical changes by imposing the coefficients from the scaling relationships obtained from our dataset, see Table S8. Also, the shape of the volcano curves and the position of the maxima remain the same. Applying the steady state approximation for each intermediate, one can solve a system of four equations and obtain the following solution at the applied voltage $V = 1.23$ V

$$v = [e^{14.23+0.5\Delta G_1/k_b T}]/[1 + 2e^{28.46} + 2e^{14.23+\Delta G_1/k_b T}$$
$$+ e^{14.23+2\Delta G_1/k_b T} + 2e^{28.46+\Delta G_1/k_b T} + e^{28.46-\Delta G_1/k_b T}$$
$$+ e^{28.46+2\Delta G_1/k_b T}] \tag{16}$$

This allows us to obtain the volcano plot reported in Figure 5a, where the ideal situation corresponds to $\Delta G_{OH} = 0$ eV at $V = 1.23$ V. One must consider that we are assuming to work under an applied voltage of 1.23 V; therefore, the optimum OH* Gibbs energy is $\Delta G_{OH} = 1.23$ eV, which is rather similar to the 1.4 eV value reported by Zhang et al that used experimentally fitted binding energies to study the kinetic problem.[82] If one takes into account the superoxo and peroxo complex formation, an additional intermediate must be included in the set of equations, with a Gibbs energy ΔG_4 (eq 10), giving rise to the following solution

$$v = e^{14.23+0.5\Delta G_1/k_b T+0.5\Delta G_4/k_b T}/(1 + e^{\Delta G_4/k_b T}$$
$$+ e^{28.46-\Delta G_1/k_b T+\Delta G_4/k_b T} + e^{28.46+\Delta G_1/k_b T}$$
$$+ e^{28.46+\Delta G_1/k_b T+\Delta G_4/k_b T} + e^{14.23+0.5\Delta G_1/k_b T+\Delta G_4/k_b T}$$
$$+ e^{42.69-0.5\Delta G_1/k_b T+\Delta G_4/k_b T} + e^{28.46+0.5\Delta G_4/k_b T}$$
$$+ e^{14.23+2\Delta G_1/k_b T+0.5\Delta G_4/k_b T} + 2e^{14.23+\Delta G_1/k_b T+0.5\Delta G_4/k_b T}$$
$$+ e^{42.69+0.5\Delta G_1/k_b T+\Delta G_4/k_b T} + e^{28.46+\Delta G_1/k_b T+0.5\Delta G_4/k_b T}$$
$$+ e^{28.46+2\Delta G_1/k_b T+0.5\Delta G_4/k_b T} + e^{42.69+1.5\Delta G_1/k_b T+\Delta G_4/k_b T}) \tag{17}$$

The full derivation of both models can be found in section S3 of the SI. Interestingly, also this equation results in a volcano plot, which, however, is now three-dimensional (3D) since it depends on two variables, ΔG_1 and ΔG_4. The maximum is characterized on one hand by the same ΔG_1 of the previous model ($\Delta G_1 = 1.23$ eV at $V = 0$ V), implying that the optimum

stability of OH, O, and OOH is the same. On the other hand, the superoxo/peroxo complex should be slightly more stable than a free O_2 molecule but not too strongly bound to avoid the necessity to overcome a large barrier for O_2 desorption, see Figure S5. According to eq 17, the optimum condition (corresponding to the apex of the volcano plot) is located sharply in one direction, $\Delta G_1 = \Delta G_{OH} = 0$ eV at $V = 1.23$ V (Figure 5b), and the other direction of the plot shows a large range of ΔG_4 values around = −1.0/−1.2 eV. Considering that a value of $\Delta G_4 = -0.74$ eV would imply a superoxo/peroxo complex isoenergetic to an isolated O_2 molecule, the top of the 3D volcano plot corresponds to have a superoxo/peroxo complex weakly bound to the catalyst. The more negative is ΔG_4, the more strongly bound is the superoxo/peroxo adduct, with consequent negative effects on the kinetics. It must be said that the kinetic models have the purpose of providing an indication of the impact of superoxo and peroxo species given the number of approximations intrinsic to the approach, while for quantitative estimates, one should include several other effects such as solvent and pH.

It is then possible to compare the calculated velocities with the two models, without and with the formation of the complex. To do so, each volcano plot is constructed by plotting $\log(v/v_{max})$, where v_{max} corresponds to the apex of the volcano plot. In this way, the maximum of the function is equal to zero, and the more negative is $\log(v/v_{max})$, the lower the catalyst activity. Using the classical model (no superoxo/peroxo complex), Co@4N-Gr is expected to be active, Mn and Fe show weak activities, and the remaining SACs, Sc, Ti, V, and Cr are predicted to be inactive, due to the high stability of some intermediates, Table 3. When the complex is included in the model, the most active SAC is still Co@4N-Gr, and the predicted activity increases by about a hundred times, see Table 3. Even larger is the effect of the formation of the superoxo/peroxo complex for Sc@4N-Gr, Cr@4N-Gr, Mn@4N-Gr, and Fe@4N-Gr catalysts since the activity increases by four to eight orders of magnitude. On the contrary, for Ti@4N-Gr and V@4N-Gr, the activity is expected to deteriorate (by two and ten orders of magnitude, respectively). Thus, great changes are expected in the kinetics of the process when the formation of the new intermediate is considered. Let us mention once more that the goal of this work is not to provide an accurate estimate of the best catalyst for OER but simply to establish the impact of the formation of a superoxo/peroxo complex. Several effects are not considered here (solvent effect, role of the functional, role of pH, etc.),[83,84] so the values reported in Table 3 should be considered as crude estimates. Neglecting the formation of these species is yet another

approximation that can lead to highly inaccurate predictions of the activity of a given SAC. One last consideration is the effect of the adopted functional. Table S7 reports the same values obtained with the PBE + U functional. As expected, there are sizeable changes in the reaction rates when comparing PBE and PBE + U, but most importantly, there are very large differences in the predicted rates if one neglects the formation of superoxo and peroxo complexes at both levels of theory. This corroborates the findings on the importance of superoxo/peroxo complexes, and suggests that one should adopt self-interaction corrected functionals, such as hybrid functionals, to provide accurate data to be compared with experiments.

4. CONCLUSIONS

We have studied the OER on single-atom catalysts consisting of TM atoms incorporated in nitrogen-doped graphene (TM@4N-Gr) by means of density functional theory. The novelty of the study lies in the fact that we explicitly considered the possible formation of end-on (superoxo) or side-on (peroxo) complexes before the O_2 molecule desorbs from the catalyst. Surprisingly, this step is neglected in the commonly reported theoretical analyses and screenings of reactivity of SACs in OER based on the fact that this species is not observed on metal surfaces, and the classical mechanism for OER, formulated for metal electrodes, does not include this possibility. However, the fact that stable superoxo/peroxo complexes form on coordination compounds is well known, and it is described in detail in coordination chemistry textbooks.

Studying the structure, stability, and electronic properties of the complexes on a series of SACs, we found that they form in most of the cases examined, providing another evidence of the strong analogies existing between SACs and transition metal complexes. The next step has been the analysis of the impact that the formation of this new intermediate has on the kinetic of the process.

To this end, we first determined the Gibbs energy profiles for the various SACs where a superoxo or peroxo complex forms, and then we developed a new microkinetic model to account for this additional step in the reaction. The results show that the complexes affect the predicted activity in a non-negligible way; the effect can be beneficial or detrimental depending on the nature of the transition metal, but it can result in changes of several orders of magnitude in the expected reaction rate (both increase and decrease are possible with respect to the classical model where superoxo is not considered). Once established the important role of superoxo and peroxo species, further work will be dedicated in the future to understand if the Gibbs energy can be rationalized in terms of scaling relations with the Gibbs energy of conventional intermediates. Indeed, some interesting correlation seems to exist between superoxo/peroxo complexes and OH* intermediates but with different features, as reported in Figure S6. The understanding and unveiling of such relations could help to simplify the problem. This requires searching for general rules and exploring a sufficiently large set of data.

The scope of the work is thus not to provide predictions for particularly active SACs for OER but just to underline the fact that the classical model that works well for metal electrodes should be used with care when transferred to the study of SACs. Our analysis clearly shows that studies of new catalysts that do not include the possible formation of superoxo and peroxo species could result in largely inaccurate predictions of

the catalytic activity. This is just another contribution showing that the chemistry of SACs is closer to that of coordination compounds than of conventional solid catalysts. Finally, we remark that the presented results are obtained by neglecting other parallel reactions that under working reactions could involve the supporting matrix. In addition to pH and solvent effects, one should also consider this effect to improve the modeling approach.

■ ASSOCIATED CONTENT

ⓢ Supporting Information

The Supporting Information is available free of charge at https://pubs.acs.org/doi/10.1021/acscatal.2c03020.

> Details regarding the simulated superoxo and peroxo adducts and derivation of the kinetic models. Supporting Tables and Figures (PDF)

■ AUTHOR INFORMATION

Corresponding Author

Giovanni Di Liberto − *Dipartimento di Scienza dei Materiali, Università di Milano—Bicocca, 20125 Milano, Italy;* ⓞ orcid.org/0000-0003-4289-2732; Email: giovanni.diliberto@unimib.it

Authors

Luis A. Cipriano − *Dipartimento di Scienza dei Materiali, Università di Milano—Bicocca, 20125 Milano, Italy;* ⓞ orcid.org/0000-0002-3801-7751

Gianfranco Pacchioni − *Dipartimento di Scienza dei Materiali, Università di Milano—Bicocca, 20125 Milano, Italy;* ⓞ orcid.org/0000-0002-4749-0751

Complete contact information is available at: https://pubs.acs.org/10.1021/acscatal.2c03020

Author Contributions

The manuscript was written through contributions of all authors.

Notes

The authors declare no competing financial interest.

■ ACKNOWLEDGMENTS

■ REFERENCES

(1) Kim, J. H.; Hansora, D.; Sharma, P.; Jang, J. W.; Lee, J. S. Toward Practical Solar Hydrogen Production-an Artificial Photosynthetic Leaf-to-Farm Challenge. *Chem. Soc. Rev.* **2019**, *48*, 1908−1971.

(2) Walter, M. G.; Warren, E. L.; McKone, J. R.; Boettcher, S. W.; Mi, Q.; Santori, E. A.; Lewis, N. S. Solar Water Splitting Cells. *Chem. Rev.* **2010**, *110*, 6446−6473.

(3) Zou, X.; Zhang, Y. Noble Metal-Free Hydrogen Evolution Catalysts for Water Splitting. *Chem. Soc. Rev.* **2015**, *44*, 5148−5180.

(4) Kudo, A.; Miseki, Y. Heterogeneous Photocatalyst Materials for Water Splitting. *Chem. Soc. Rev.* **2009**, *38*, 253−278.

(5) Koper, M. T. M. Activity Volcanoes for the Electrocatalysis of Homolytic and Heterolytic Hydrogen Evolution. *J. Solid State Electrochem.* **2016**, *20*, 895−899.

(6) Nørskov, J. K.; Bligaard, T.; Logadottir, A.; Kitchin, J. R.; Chen, J. G.; Pandelov, S.; Stimming, U. Trends in the Exchange Current for Hydrogen Evolution. *J. Electrochem. Soc.* **2005**, *152*, No. J23.

(7) Rossmeisl, J.; Logadottir, A.; Nørskov, J. K. Electrolysis of Water on (Oxidized) Metal Surfaces. *Chem. Phys.* **2005**, *319*, 178−184.

(8) Rossmeisl, J.; Qu, Z.-W.; Zhu, H.; Kroes, G.-J.; Nørskov, J. K. Electrolysis of Water on Oxide Surfaces. *J. Electroanal. Chem.* **2007**, *607*, 83−89.

(9) Man, I. C.; Su, H.; Calle-Vallejo, F.; Hansen, H. A.; Martínez, J. I.; Inoglu, N. G.; Kitchin, J.; Jaramillo, T. F.; Nørskov, J. K.; Rossmeisl, J. Universality in Oxygen Evolution Electrocatalysis on Oxide Surfaces. *ChemCatChem* **2011**, *3*, 1159−1165.

(10) Seh, Z. W.; Kibsgaard, J.; Dickens, C. F.; Chorkendorff, I.; Nørskov, J. K.; Jaramillo, T. F. Combining Theory and Experiment in Electrocatalysis: Insights into Materials Design. *Science* **2017**, *355*, No. eaad4998.

(11) Heard, D. M.; Lennox, A. J. J. Electrode Materials in Modern Organic Electrochemistry. *Angew. Chem., Int. Ed.* **2020**, *59*, 18866−18884.

(12) Koper, M. T. M. Thermodynamic Theory of Multi-Electron Transfer Reactions: Implications for Electrocatalysis. *J. Electroanal. Chem.* **2011**, *660*, 254−260.

(13) Suen, N.-T.; Hung, S.-F.; Quan, Q.; Zhang, N.; Xu, Y.-J.; Chen, H. M. Electrocatalysis for the Oxygen Evolution Reaction: Recent Development and Future Perspectives. *Chem. Soc. Rev.* **2017**, *46*, 337−365.

(14) Fabbri, E.; Schmidt, T. J. Oxygen Evolution Reaction—The Enigma in Water Electrolysis. *ACS Catal.* **2018**, *8*, 9765−9774.

(15) Zhang, L.; Jia, Y.; Gao, G.; Yan, X.; Chen, N.; Chen, J.; Soo, M. T.; Wood, B.; Yang, D.; Du, A.; et al. Graphene Defects Trap Atomic Ni Species for Hydrogen and Oxygen Evolution Reactions. *Chem* **2018**, *4*, 285−297.

(16) Vonrüti, N.; Rao, R.; Giordano, L.; Shao-Horn, Y.; Aschauer, U. Implications of Nonelectrochemical Reaction Steps on the Oxygen Evolution Reaction: Oxygen Dimer Formation on Perovskite Oxide and Oxynitride Surfaces. *ACS Catal.* **2022**, *12*, 1433−1442.

(17) Montoya, J. H.; Doyle, A. D.; Nørskov, J. K.; Vojvodic, A. Trends in Adsorption of Electrocatalytic Water Splitting Intermediates on Cubic ABO$_3$ Oxides. *Phys. Chem. Chem. Phys.* **2018**, *20*, 3813−3818.

(18) Lee, Y.-L.; Gadre, M. J.; Shao-Horn, Y.; Morgan, D. Ab Initio GGA+*U* Study of Oxygen Evolution and Oxygen Reduction Electrocatalysis on the (001) Surfaces of Lanthanum Transition Metal Perovskites LaBO$_3$ (B = Cr, Mn, Fe, Co and Ni). *Phys. Chem. Chem. Phys.* **2015**, *17*, 21643−21663.

(19) Kim, H. Y.; Henkelman, G. CO Oxidation at the Interface of Au Nanoclusters and the Stepped-CeO$_2$ (111) Surface by the Mars−van Krevelen Mechanism. *J. Phys. Chem. Lett.* **2013**, *4*, 216−221.

(20) Schlexer, P.; Widmann, D.; Behm, R. J.; Pacchioni, G. CO Oxidation on a Au/TiO$_2$ Nanoparticle Catalyst via the Au-Assisted Mars−van Krevelen Mechanism. *ACS Catal.* **2018**, *8*, 6513−6525.

(21) Wang, T.; Zhang, Y.; Huang, B.; Cai, B.; Rao, R. R.; Giordano, L.; Sun, S. G.; Shao-Horn, Y. Enhancing Oxygen Reduction Electrocatalysis by Tuning Interfacial Hydrogen Bonds. *Nat. Catal.* **2021**, *4*, 753−762.

(22) Rao, R. R.; Kolb, M. J.; Halck, N. B.; Pedersen, A. F.; Mehta, A.; You, H.; Stoerzinger, K. A.; Feng, Z.; Hansen, H. A.; Zhou, H.; et al. Towards Identifying the Active Sites on RuO$_2$ (110) in Catalyzing Oxygen Evolution. *Energy Environ. Sci.* **2017**, *10*, 2626−2637.

(23) Zagalskaya, A.; Alexandrov, V. Role of Defects in the Interplay between Adsorbate Evolving and Lattice Oxygen Mechanisms of the Oxygen Evolution Reaction in RuO$_2$ and IrO$_2$. *ACS Catal.* **2020**, *10*, 3650−3657.

(24) Zhu, C.; Shi, Q.; Feng, S.; Du, D.; Lin, Y. Single-Atom Catalysts for Electrochemical Water Splitting. *ACS Energy Lett.* **2018**, *3*, 1713−1721.

(25) Zhang, Q.; Guan, J. Single-Atom Catalysts for Electrocatalytic Applications. *Adv. Funct. Mater.* **2020**, *30*, No. 2000768.

(26) Qiao, W.; Xu, W.; Xu, X.; Wu, L.; Yan, S.; Wang, D. Construction of Active Orbital via Single-Atom Cobalt Anchoring on the Surface of 1T-MoS$_2$ Basal Plane toward Efficient Hydrogen Evolution. *ACS Appl. Energy Mater.* **2020**, *3*, 2315−2322.

(27) Hossain, M. D.; Liu, Z.; Zhuang, M.; Yan, X.; Xu, G.-L.; Gadre, C. A.; Tyagi, A.; Abidi, I. H.; Sun, C.-J.; Wong, H.; et al. Rational Design of Graphene-Supported Single Atom Catalysts for Hydrogen Evolution Reaction. *Adv. Energy Mater.* **2019**, *9*, No. 1803689.

(28) Qiao, B.; Wang, A.; Yang, X.; Allard, L. F.; Jiang, Z.; Cui, Y.; Liu, J.; Li, J.; Zhang, T. Single-Atom Catalysis of CO Oxidation Using Pt1/FeOx. *Nat. Chem.* **2011**, *3*, 634−641.

(29) Lin, Z.; Escudero-Escribano, M.; Li, J. Recent Progress and Perspectives on Single-Atom Catalysis. *J. Mater. Chem. A* **2022**, *10*, 5670−5672.

(30) Vilé, G.; Di Liberto, G.; Tosoni, S.; Sivo, A.; Ruta, V.; Nachtegaal, M.; Clark, A. H.; Agnoli, S.; Zou, Y.; Savateev, A.; et al. Azide-Alkyne Click Chemistry over a Heterogeneous Copper-Based Single-Atom Catalyst. *ACS Catal.* **2022**, *12*, 2947−2958.

(31) Liu, L.; Corma, A. Confining Isolated Atoms and Clusters in Crystalline Porous Materials for Catalysis. *Nat. Rev. Mater.* **2021**, *6*, 244−263.

(32) Van Dao, D.; Cipriano, L. A.; Di Liberto, G.; Nguyen, T. T. D.; Ki, S.-W.; Son, H.; Kim, G.-C.; Lee, K. H.; Yang, J.-K.; Yu, Y.-T.; et al. Plasmonic Au Nanoclusters Dispersed in Nitrogen-Doped Graphene as a Robust Photocatalyst for Light-to-Hydrogen Conversion. *J. Mater. Chem. A* **2021**, *9*, 22810−22819.

(33) Tang, Y.; Asokan, C.; Xu, M.; Graham, G. W.; Pan, X.; Christopher, P.; Li, J.; Sautet, P. Rh Single Atoms on TiO2 Dynamically Respond to Reaction Conditions by Adapting Their Site. *Nat. Commun.* **2019**, *10*, 4488.

(34) Cheng, N.; Stambula, S.; Wang, D.; Banis, M. N.; Liu, J.; Riese, A.; Xiao, B.; Li, R.; Sham, T.-K.; Liu, L.-M.; et al. Platinum Single-Atom and Cluster Catalysis of the Hydrogen Evolution Reaction. *Nat. Commun.* **2016**, *7*, 13638.

(35) Di Liberto, G.; Cipriano, L. A.; Pacchioni, G. Role of Dihydride and Dihydrogen Complexes in Hydrogen Evolution Reaction on Single-Atom Catalysts. *J. Am. Chem. Soc.* **2021**, *143*, 20431−20441.

(36) MINGOS, D. M. P. Geometries of Dioxygen (O2), Superoxo (O2−) and Peroxo (O22−) Complexes. *Nat. Phys. Sci.* **1971**, *230*, 154−156.

(37) Bytheway, I.; Hall, M. B. Theoretical Calculations of Metal-Dioxygen Complexes. *Chem. Rev.* **1994**, *94*, 639−658.

(38) Martell, A. E. Formation and Stabilities of Cobalt Dioxygen Complexes in Aqueous Solution. *Acc. Chem. Res.* **1982**, *15*, 155−162.

(39) Ackers, G. K.; Holt, J. M. Asymmetric Cooperativity in a Symmetric Tetramer: Human Hemoglobin. *J. Biol. Chem.* **2006**, *281*, 11441−11443.

(40) Poulos, T. L. Heme Enzyme Structure and Function. *Chem. Rev.* **2014**, *114*, 3919−3962.

(41) Chen, Y.; Ji, S.; Wang, Y.; Dong, J.; Chen, W.; Li, Z.; Shen, R.; Zheng, L.; Zhuang, Z.; Wang, D.; et al. Isolated Single Iron Atoms Anchored on N-Doped Porous Carbon as an Efficient Electrocatalyst for the Oxygen Reduction Reaction. *Angew. Chem.* **2017**, *129*, 7041−7045.

(42) Jiao, L.; Yan, H.; Wu, Y.; Gu, W.; Zhu, C.; Du, D.; Lin, Y. When Nanozymes Meet Single-Atom Catalysis. *Angew. Chem.* **2020**, *132*, 2585−2596.

(43) Cao, H.; Xia, G.-J.; Chen, J.-W.; Yan, H.-M.; Huang, Z.; Wang, Y.-G. Mechanistic Insight into the Oxygen Reduction Reaction on the Mn−N$_4$/C Single-Atom Catalyst: The Role of the Solvent Environment. *J. Phys. Chem. C* **2020**, *124*, 7287−7294.

(44) Wang, Y.; Yuan, H.; Li, Y.; Chen, Z. Two-Dimensional Iron-Phthalocyanine (Fe-Pc) Monolayer as a Promising Single-Atom-Catalyst for Oxygen Reduction Reaction: A Computational Study. *Nanoscale* **2015**, *7*, 11633−11641.

(45) Datta, J.; Majumder, C. Stabilizing Co, Ni and Cu on the h-BN Surface: Using O O Bond Activation to Probe Their Performance as Single Atom Catalyst. *Catal. Today* **2021**, *370*, 75−82.

(46) Fukuzumi, S.; Lee, Y.-M.; Nam, W. Structure and Reactivity of the First-Row d-Block Metal-Superoxo Complexes. *Dalton Trans.* **2019**, *48*, 9469−9489.

(47) Xu, H.; Cheng, D.; Cao, D.; Zeng, X. C. A Universal Principle for a Rational Design of Single-Atom Electrocatalysts. *Nat. Catal.* **2018**, *1*, 339−348.

(48) Fei, H.; Dong, J.; Arellano-Jiménez, M. J.; Ye, G.; Dong Kim, N.; Samuel, E. L. G.; Peng, Z.; Zhu, Z.; Qin, F.; Bao, J.; et al. Atomic Cobalt on Nitrogen-Doped Graphene for Hydrogen Generation. *Nat. Commun.* **2015**, *6*, No. 8668.

(49) Fei, H.; Dong, J.; Wan, C.; Zhao, Z.; Xu, X.; Lin, Z.; Wang, Y.; Liu, H.; Zang, K.; Luo, J.; et al. Microwave-Assisted Rapid Synthesis of Graphene-Supported Single Atomic Metals. *Adv. Mater.* **2018**, *30*, No. 1802146.

(50) Fei, H.; Dong, J.; Chen, D.; Hu, T.; Duan, X.; Shakir, I.; Huang, Y.; Duan, X. Single Atom Electrocatalysts Supported on Graphene or Graphene-like Carbons. *Chem. Soc. Rev.* **2019**, *48*, 5207−5241.

(51) Kresse, G.; Hafner, J. Ab Initio Molecular Dynamics for Liquid Metals. *Phys. Rev. B* **1993**, *47*, 558−561.

(52) Kresse, G.; Hafner, J. Ab Initio Molecular-Dynamics Simulation of the Liquid-Metal−Amorphous-Semiconductor Transition in Germanium. *Phys. Rev. B* **1994**, *49*, 14251−14269.

(53) Kresse, G.; Furthmüller, J. Efficiency of Ab-Initio Total Energy Calculations for Metals and Semiconductors Using a Plane-Wave Basis Set. *Comput. Mater. Sci.* **1996**, *6*, 15−50.

(54) Perdew, J. P.; Burke, K.; Ernzerhof, M. Generalized Gradient Approximation Made Simple. *Phys. Rev. Lett.* **1996**, *77*, 3865−3868.

(55) Grimme, S.; Antony, J.; Ehrlich, S.; Krieg, H. A Consistent and Accurate Ab Initio Parametrization of Density Functional Dispersion Correction (DFT-D) for the 94 Elements H-Pu. *J. Chem. Phys.* **2010**, *132*, No. 154104.

(56) Blöchl, P. E. Projector Augmented-Wave Method. *Phys. Rev. B* **1994**, *50*, 17953−17979.

(57) Kresse, G.; Joubert, D. From Ultrasoft Pseudopotentials to the Projector Augmented-Wave Method. *Phys. Rev. B* **1999**, *59*, 1758−1775.

(58) Monkhorst, H. J.; Pack, J. D. Special Points for Brillouin-Zone Integrations. *Phys. Rev. B* **1976**, *13*, 5188−5192.

(59) Van Dao, D.; Di Liberto, G.; Ko, H.; Park, J.; Wang, W.; Shin, D.; Son, H.; Van Le, Q.; Van Nguyen, T.; Van Tan, V.; et al. LaFeO₃ Meets Nitrogen-Doped Graphene Functionalized with Ultralow Pt Loading in an Impactful Z-Scheme Platform for Photocatalytic Hydrogen Evolution. *J. Mater. Chem. A* **2022**, *10*, 3330−3340.

(60) Patel, A. M.; Ringe, S.; Siahrostami, S.; Bajdich, M.; Nørskov, J. K.; Kulkarni, A. R. Theoretical Approaches to Describing the Oxygen Reduction Reaction Activity of Single-Atom Catalysts. *J. Phys. Chem. C* **2018**, *122*, 29307−29318.

(61) Dudarev, S. L.; Botton, G. A.; Savrasov, S. Y.; Humphreys, C. J.; Sutton, A. P. Electron-Energy-Loss Spectra and the Structural Stability of Nickel Oxide: An LSDA+U Study. *Phys. Rev. B* **1998**, *57*, 1505−1509.

(62) Liechtenstein, A. I.; Anisimov, V. I.; Zaanen, J. Density-Functional Theory and Strong Interactions: Orbital Ordering in Mott-Hubbard Insulators. *Phys. Rev. B* **1995**, *52*, R5467−R5470.

(63) Kulik, H. J.; Cococcioni, M.; Scherlis, D. A.; Marzari, N. Density Functional Theory in Transition-Metal Chemistry: A Self-Consistent Hubbard U Approach. *Phys. Rev. Lett.* **2006**, *97*, No. 103001.

(64) Gong, L.; Zhang, D.; Lin, C.; Zhu, Y.; Shen, Y.; Zhang, J.; Han, X.; Zhang, L.; Xia, Z. Catalytic Mechanisms and Design Principles for Single-Atom Catalysts in Highly Efficient CO₂ Conversion. *Adv. Energy Mater.* **2019**, *9*, No. 1902625.

(65) Lin, C.; Zhang, L.; Zhao, Z.; Xia, Z. Design Principles for Covalent Organic Frameworks as Efficient Electrocatalysts in Clean Energy Conversion and Green Oxidizer Production. *Adv. Mater.* **2017**, *29*, No. 1606635.

(66) Solovyev, I. V.; Dederichs, P. H.; Anisimov, V. I. Corrected Atomic Limit in the Local-Density Approximation and the Electronic Structure of d Impurities in Rb. *Phys. Rev. B* **1994**, *50*, 16861−16871.

(67) Di Liberto, G.; Cipriano, L. A.; Pacchioni, G. Universal Principles for the Rational Design of Single Atom Electrocatalysts? Handle with Care. *ACS Catal.* **2022**, 5846−5856.

(68) Berry, R. E. 1.32 - Reactivity and Structure of Complexes of Small Molecules: Dioxygen. In *Comprehensive Coordination Chemistry II*; McCleverty, J. A.; Meyer, T. J., Eds.; Pergamon: Oxford, 2003; pp 625−629, DOI: 10.1016/B0-08-043748-6/01161-0.

(69) Unno, M.; Chen, H.; Kusama, S.; Shaik, S.; Ikeda-Saito, M. Structural Characterization of the Fleeting Ferric Peroxo Species in Myoglobin: Experiment and Theory. *J. Am. Chem. Soc.* **2007**, *129*, 13394−13395.

(70) Chen, H.; Ikeda-Saito, M.; Shaik, S. Nature of the Fe−O2 Bonding in Oxy-Myoglobin: Effect of the Protein. *J. Am. Chem. Soc.* **2008**, *130*, 14778−14790.

(71) Li, J.; Noll, B. C.; Oliver, A. G.; Schulz, C. E.; Scheidt, W. R. Correlated Ligand Dynamics in Oxyiron Picket Fence Porphyrins: Structural and Mössbauer Investigations. *J. Am. Chem. Soc.* **2013**, *135*, 15627−15641.

(72) Armillotta, F.; Pividori, A.; Stredansky, M.; Seriani, N.; Vesselli, E. Dioxygen at Biomimetic Single Metal-Atom Sites: Stabilization or Activation? The Case of CoTPyP/Au(111). *Top. Catal.* **2020**, *63*, 1585−1595.

(73) Collman, J. P.; Gagne, R. R.; Reed, C.; Halbert, T. R.; Lang, G.; Robinson, W. T. Picket Fence Porphyrins. Synthetic Models for Oxygen Binding Hemoproteins. *J. Am. Chem. Soc.* **1975**, *97*, 1427−1439.

(74) Huang, X.; Groves, J. T. Oxygen Activation and Radical Transformations in Heme Proteins and Metalloporphyrins. *Chem. Rev.* **2018**, *118*, 2491−2553.

(75) Anneser, M. R.; Haslinger, S.; Pöthig, A.; Cokoja, M.; D'Elia, V.; Högerl, M. P.; Basset, J.-M.; Kühn, F. E. Binding of Molecular Oxygen by an Artificial Heme Analogue: Investigation on the Formation of an Fe−Tetracarbene Superoxo Complex. *Dalt. Trans.* **2016**, *45*, 6449−6455.

(76) Hong, S.; Sutherlin, K. D.; Park, J.; Kwon, E.; Siegler, M. A.; Solomon, E. I.; Nam, W. Crystallographic and Spectroscopic Characterization and Reactivities of a Mononuclear Non-Haem Iron(III)-Superoxo Complex. *Nat. Commun.* **2014**, *5*, No. 5440.

(77) Zhong, L.; Li, S. Unconventional Oxygen Reduction Reaction Mechanism and Scaling Relation on Single-Atom Catalysts. *ACS Catal.* **2020**, *10*, 4313−4318.

(78) Greeley, J.; Stephens, I. E. L.; Bondarenko, A. S.; Johansson, T. P.; Hansen, H. A.; Jaramillo, T. F.; Rossmeisl, J.; Chorkendorff, I.; Nørskov, J. K. Alloys of Platinum and Early Transition Metals as Oxygen Reduction Electrocatalysts. *Nat. Chem.* **2009**, *1*, 552−556.

(79) Greeley, J.; Jaramillo, T. F.; Bonde, J.; Chorkendorff, I.; Nørskov, J. K. Computational High-Throughput Screening of Electrocatalytic Materials for Hydrogen Evolution. *Nat. Mater.* **2006**, *5*, 909−913.

(80) Calle-Vallejo, F.; Martínez, J. I.; García-Lastra, J. M.; Abad, E.; Koper, M. T. M. Oxygen Reduction and Evolution at Single-Metal Active Sites: Comparison between Functionalized Graphitic Materials and Protoporphyrins. *Surf. Sci.* **2013**, *607*, 47−53.

(81) Yang, X.; Xia, D.; Kang, Y.; Du, H.; Kang, F.; Gan, L.; Li, J. Unveiling the Axial Hydroxyl Ligand on Fe N 4 C Electrocatalysts and Its Impact on the PH-Dependent Oxygen Reduction Activities and Poisoning Kinetics. *Adv. Sci.* **2020**, *7*, No. 2000176.

(82) Zhang, J.; Tao, H. B.; Kuang, M.; Yang, H.; Bin; Cai, W.; Yan, Q.; Mao, Q.; Liu, B. Advances in Thermodynamic-Kinetic Model for Analyzing the Oxygen Evolution Reaction. *ACS Catal.* **2020**, *10*, 8597−8610.

(83) He, Z.-D.; Hanselman, S.; Chen, Y.-X.; Koper, M. T. M.; Calle-Vallejo, F. Importance of Solvation for the Accurate Prediction of Oxygen Reduction Activities of Pt-Based Electrocatalysts. *J. Phys. Chem. Lett.* **2017**, *8*, 2243−2246.

(84) Calle-Vallejo, F.; F de Morais, R.; Illas, F.; Loffreda, D.; Sautet, P. Affordable Estimation of Solvation Contributions to the Adsorption Energies of Oxygenates on Metal Nanoparticles. *J. Phys. Chem. C* **2019**, *123*, 5578−5582.

📖 Recommended by ACS